Supporting Information

Hydroxyl covalent organic framework integrated on functionalized graphene for enhanced electrochemical energy storage

Di Cui, [a,b] Wei Xie, [b] Shuran Zhang, [b] Nan Jiang, [b] Yanhong Xu, *[b] Zhongmin Su *[a]

[a] *Department of Chemistry, Faculty of Science, Yanbian University, Yanji, Jilin, 133002, China.*

[b] *Key Laboratory of Preparation and Applications of Environmental Friendly Materials, Key Laboratory of Functional Materials Physics and Chemistry of the Ministry of Education (Jilin Normal University), Changchun, 130103, China.*

***Corresponding Author:** Yanhong Xu, Zhongmin Su.*

***Email:** xuyh198@163.com, zmsu@nenu.edu.cn*

Section A. Material and methods

All commercially available reagents and solvents were used as received without further purification, unless otherwise noted.

Synthesis of graphene oxide (GO):[1] GO was prepared via using the modified Hummers method.[2] Typically, graphite powder (1.5 g) and $KMnO_4$ (9.0 g) was added to the mixture composed of 180 mL of concentrated H_2SO_4 and 20 mL of H_3PO_4, and then the mixture was stirred at 50 °C for 24 h. After that, 600 mL ice water (DI water) was added into the mixture, together with 1 mL of 30% H_2O_2 to a graphite oxide suspension. Then, the suspension was sonicated for 1 h and centrifuged at 1000 rpm for 10 min to attain the graphite oxide supernatant. Finally, the graphite oxide supernatant was centrifuged at 8000 rpm for 7 min. The remaining product was washed repeatedly and continuously with DI water, 30 wt.% HCl, and ethanol for 3 times respectively. A yellow-brown graphene oxide (GO) was attained and further dried using a vacuum freeze-drying device.

Synthesis of a-GO:[3] For the synthesis of the aniline functionalized graphene oxide (a-GO), 100 mg of GO was dispersed in 100 mL of H_2O by ultrasonication, and 175 mg of *p*-Phenylenediamine and 450 μL of 98 wt.% H_2SO_4 were added into the GO suspension and kept in an ice bath. Then 1 mL of $NaNO_2$ solution (8 M) was added into the above suspension under stirring for 30 min. Subsequently, the suspension was stirred at an elevated temperature of 60 ℃ for 6 h, the obtained mixture was separated by centrifugation and washed by water repeatedly. Then after being freeze-dried overnight, aniline-functionalized graphene oxide (a-GO) was obtained.

Synthesis of TAPT-DHTA-COF: To a pyrex tube (5 mL, the outer diameter is 10 mm and the inner diameter is 8 mm) was added 2,4,6-tris(4-aminophenyl)-1,3,5-triazine (TAPT, 14.2 mg, 0.04 mmol), 2,5-dihydroxyterephthalaldehyde (DHTA, 10 mg, 0.06 mmol), 6 M acetic acid (0.2 mL), 1,2-dichlorobenzene (*o*-DCB, 0.8 mL) and ethanol (EtOH, 0.2 mL). This mixture was sonicated for 20 minutes to get a homogenous dispersion. The tube was flash frozen at 77 K (liquid N_2 bath) and degassed by three freeze-pump-thaw cycles. The tube was sealed off and then heated at 120 °C for 3 days. The precipitate was collected by centrifugation, washed with THF, and dried at 120 °C under vacuum overnight to obtain TAPT-DHTA-COF in 86% yield.

Synthesis of a-rGO@TD-COF-x: A series of a-rGO@TD-COF-x were synthesized using similar methods, x represents the mass ratio of COF monomers input over a-GO ($x = m_{a\text{-}GO}/m_{TAPT}+m_{DHTA}$). Take the a-rGO@TD-COF-4 as a typical example, 48.4 mg a-GO, 7.1 mg TAPT and 5 mg DHTA were added in a pyrex tube, followed by adding 2 mL *o*-DCB/EtOH (v/v = 4/1). The mixture was sonicated for 30 min at room temperature and then 0.2 mL acetic acid (6 M) was added. The tube was degassed via three freeze-pump-thaw cycles, then placed in an oven at 120 °C for 3 days. After cooling to room temperature, the mixture was centrifuged and washed with acetone. The final solid powder was vacuum dried at 120 °C overnight. Pristine a-rGO was also prepared under the same solvothermal condition as a reference.

Material Characterizations: Fourier transforms Infrared (FT-IR) spectra were recorded on a Perkin-Elmer model FT-IR-frontier infrared spectrometer. For all FT-IR tests, a small amount

of sample can be directly mixed with potassium bromide and ground into a powder, compressed, and the pressed product can be directly tested. Solid-state ^{13}C cross-polarization/magic angle spinning nuclear magnetic resonance (CP/MAS NMR) analysis was conducted using AVANCEIII/WB-400. Field-emission scanning electron microscopy (FE-SEM) images were performed on a JEOL model JSM-6700 operating at an accelerating voltage of 5.0 kV. Powder X-ray diffraction (PXRD) data were recorded on a Rigaku model RINT Ultima III diffractometer by depositing powder on glass substrate, from $2\theta = 2.5°$ up to 40° with 0.02° increment. TGA analysis was carried out by using a Q5000IR analyzer (TA Instruments) with an automated vertical overhead thermobalance. Before measurement, the samples were heated at a rate of 10 °C min^{-1} under a nitrogen atmosphere. X-ray photoelectron spectra (XPS) were recorded on an ESCALAB250Xi electron spectrometer (Thermo Fisher Scientific Inc., Waltham, MA, USA). Raman spectra were estimated using a Via Raman spectrometer (WITec alpha300 R, 532 nm), conducted by the TESCAN RISE (S9000G). Nitrogen sorption isotherms were measured at 77 K with Bel Japan Inc. model BELSORP-max analyzer. Before measurement, the samples were degassed in vacuum at 120 °C for more than 10 h. The Brunauer-Emmett-Teller (BET) method was utilized to calculate the specific surface areas and pore volume. The nonlocal density functional theory (NLDFT) method was applied for the estimation of pore size and pore size distribution. Before measurement, the samples were also degassed in vacuum at 120 °C for more than 10 h.

Electrochemical Characterizations: In three-electrode system, the platinum wire and saturated calomel electrode were used as counter electrode and reference electrode,

respectively, and the 1.0 M H_2SO_4 was used as electrolyte. The working electrode was fabricated as followed. A piece of carbon cloth (CC, 1 cm × 2 cm) was thoroughly cleaned several times with DI water followed by ethanol; it was then dried in a vacuum oven. Using a mortar and pestle, as synthesized powder samples were mixed with Super-P conductive carbon as conductive additive and poly (vinylidene fluoride) (PVDF) as binder (weight ratio of 8:1:1) in the presence of N-methyl-2-pyrrolidone (NMP) to make a homogeneous slurry. The resultant slurry was then uniformly coated by doctor blade on the surface of freshly cleaned CC. Subsequently, it was transferred to an electric oven and dried at 60 °C overnight to be used as an electrode. The a-rGO@TD-COF-4 was employed as both negative and positive electrodes materials to assemble a symmetric supercapacitor (SSC) device. Then the two electrodes were activated in 1 M H_2SO_4 and separated by filter paper before packaged in a coin cell at room temperature with pressure. The loading mass of the a-rGO@TD-COF-4 in the positive electrode was 1–1.2 mg cm^{-2}. A series of electrochemical measuring techniques including cyclic voltammogram (CV), galvanostatic charge-discharge (GCD) and electrochemical impedance spectroscopy (EIS) which were performed on a CHI 660E electrochemical workstation (Shanghai CH Instruments, China). Cyclic voltammetry measurements were performed in the potential window of 0–1 V under various scan rates. The galvanostatic charge-discharge were tested at different constant current density and the charge/discharge potential−time curve was used to calculate capacitances based on $C = i \cdot \Delta t / \Delta V$, where C (F g^{-1}) is specific capacitance, i (A g^{-1}) represents charge/discharge current density, ΔV (V) represents the potential change during charge/discharge, Δt (s) is the total discharge time. EIS was conducted in the frequency range of 10^5 -10^{-2} Hz with an amplitude

of 5 mV. Cycling stability was measured by using a CT4008T Land battery tester (Wuhan Landian Electronic Co., China). The energy densities E (Wh kg^{-1}) and power densities P (W kg^{-1}) for the supercapacitors were calculated from galvanostatic charge-discharge curves using the equations ($E = C \cdot \Delta V^2 /7.2$ and $P = E/\Delta t$).

Section B. FT-IR spectra

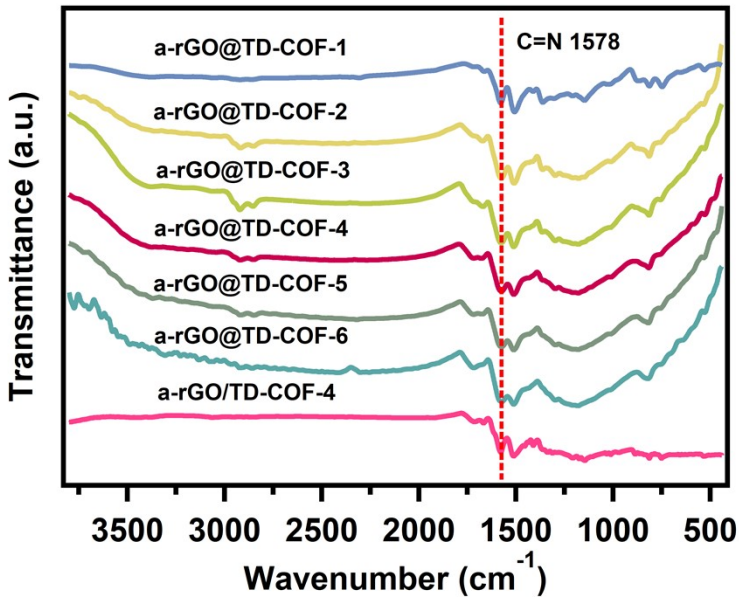

Fig. S1 FT-IR spectra of a-rGO@TD-COF-1-6 and a-rGO/TD-COF-4.

Section C. Raman spectra

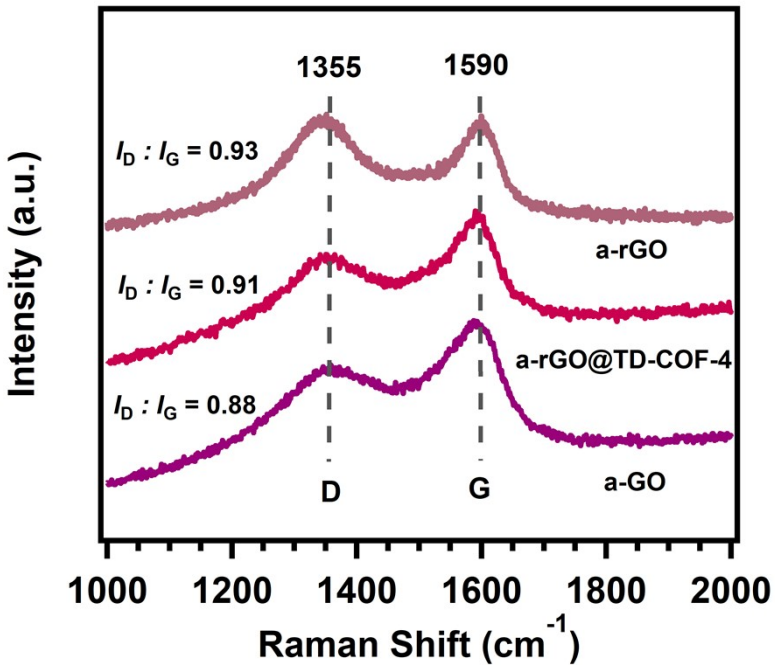

Fig. S2 Raman spectra of a-GO, a-rGO and a-rGO@TD-COF-4.

Section D. ^{13}C NMR spectrum

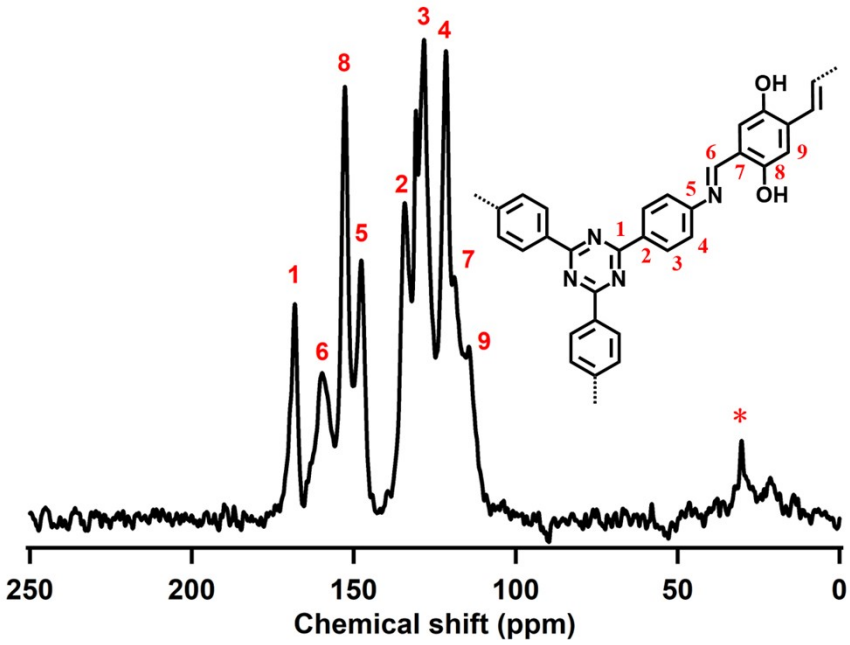

Fig. S3 ^{13}C NMR spectrum of TATP-DHTA-COF.

Section E. XRD patterns

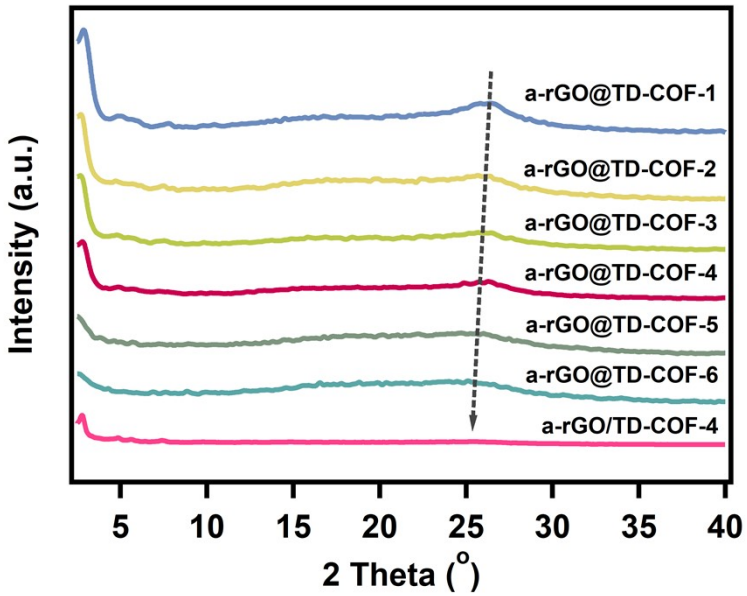

Fig. S4 XRD patterns of a-rGO@TD-COF-1-6 and a-rGO/TD-COF-4.

Section F. SEM images

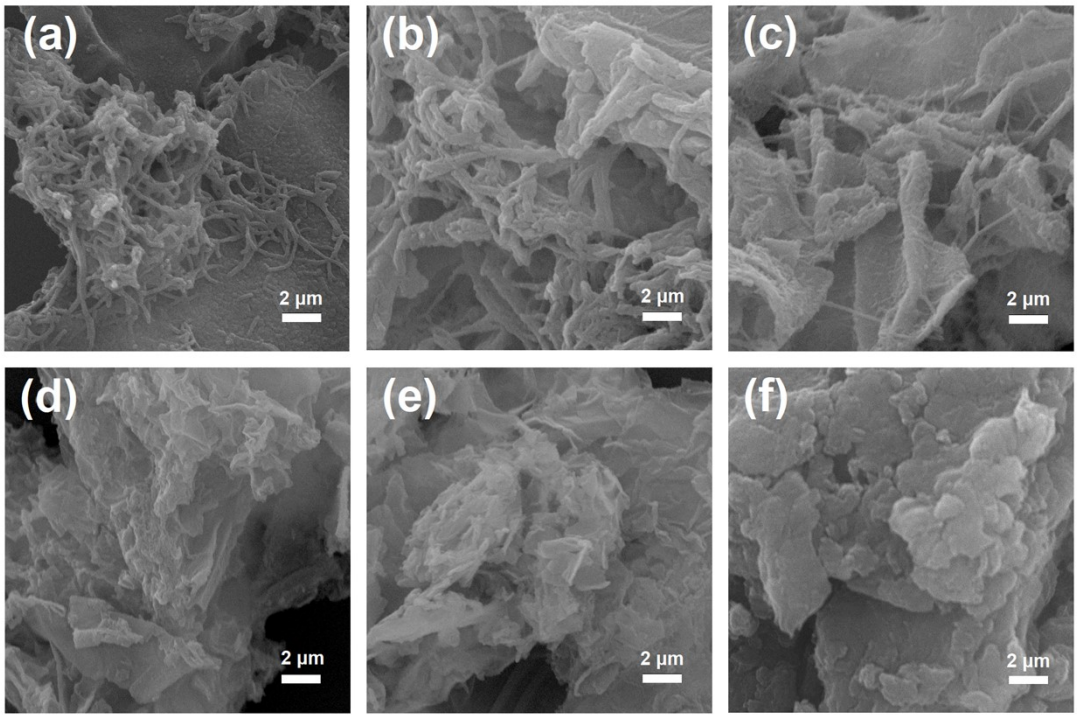

Fig. S5 SEM images of (a-c) a-rGO@TD-COF-1-3, (d-e) a-rGO@TD-COF-5-6 and (f) a-rGO/TD-COF-4.

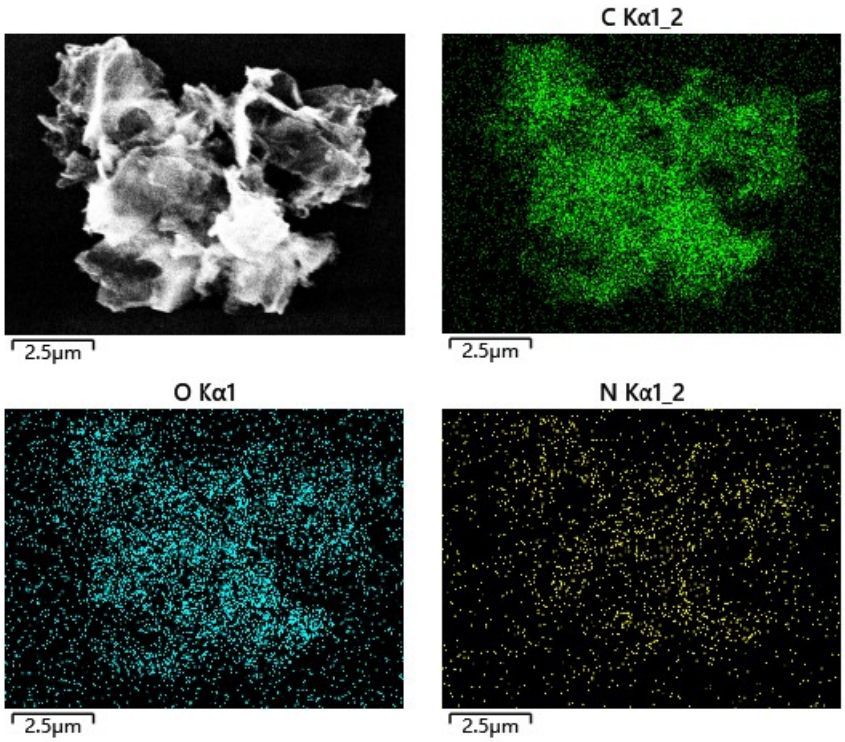

Fig. S6 Elemental mapping of a-rGO@TD-COF-4.

Section G. TGA curves

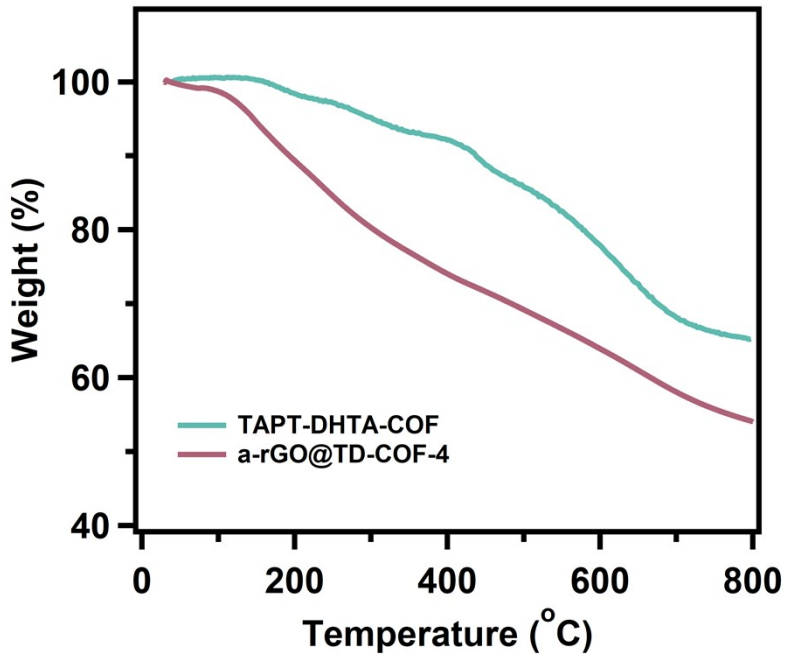

Fig. S7 TGA curves of TAPT-DHTA-COF and a-rGO@TD-COF-4.

Section H. XPS spectra

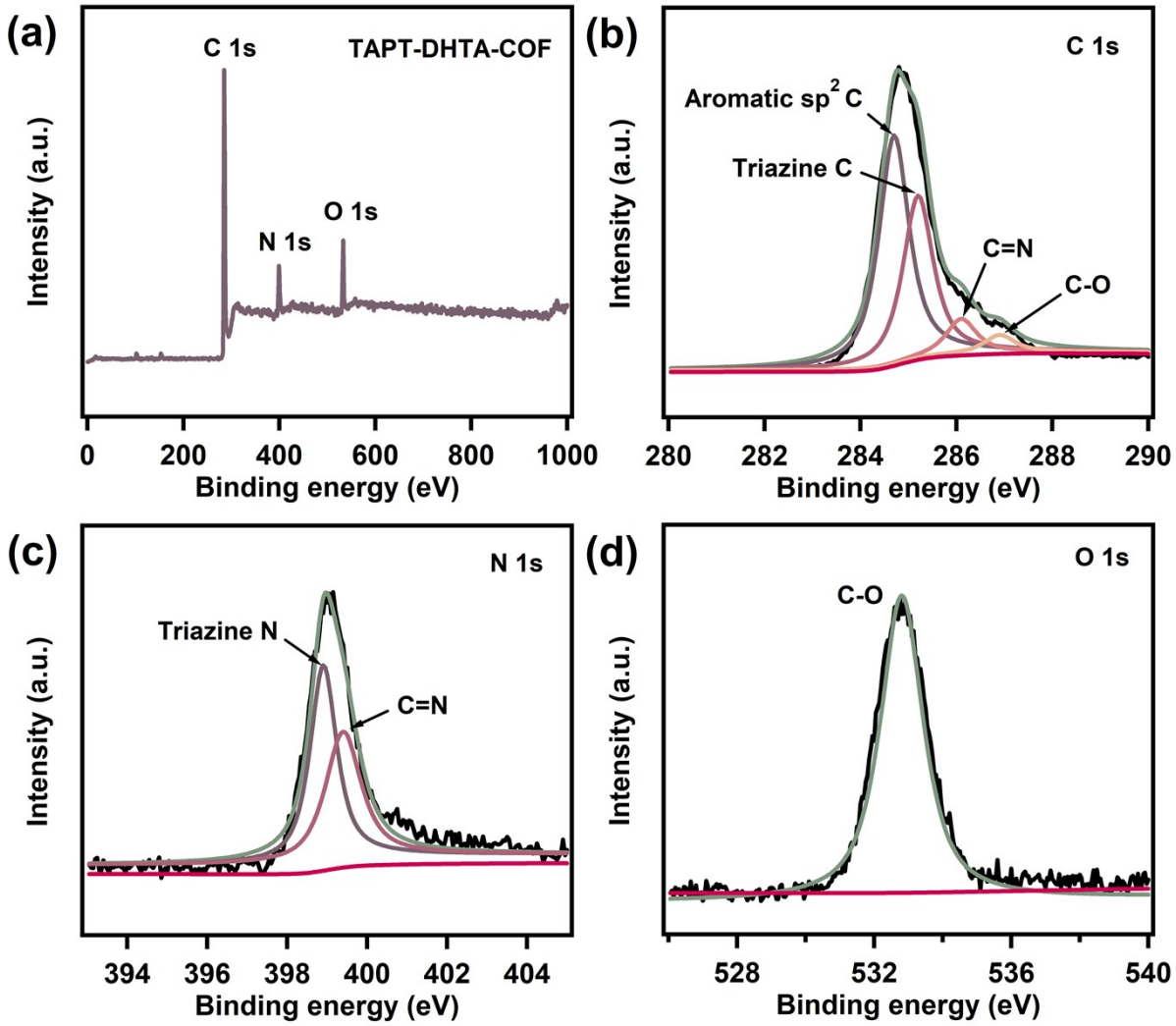

Fig. S8 (a) XPS survey spectrum for TAPT-DHTA-COF. High-resolution XPS spectra of the (b) C 1s, (c) N 1s and (d) O 1s of TAPT-DHTA-COF.

Section I. N_2 adsorption isotherms and pore size distributions

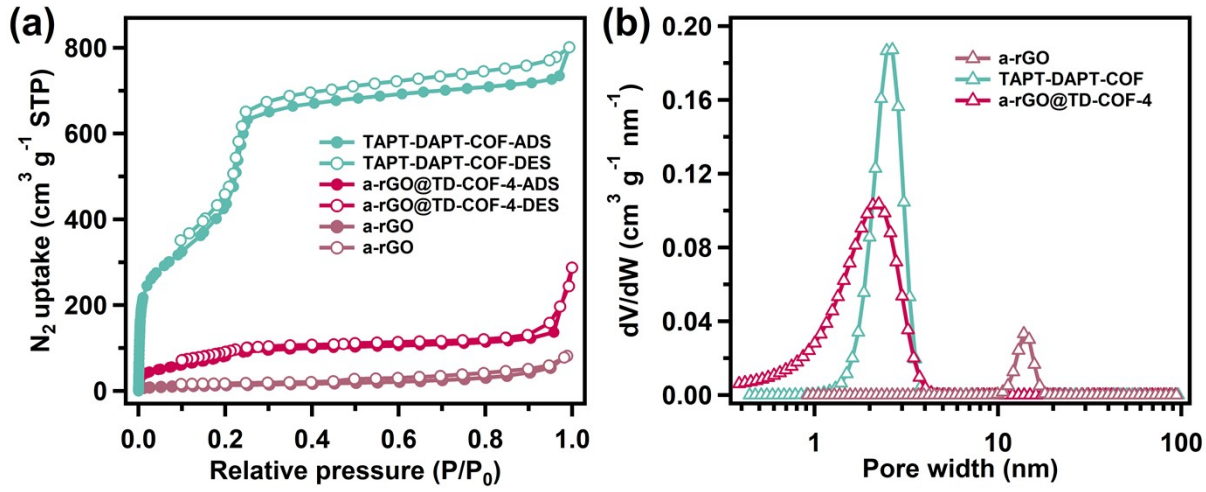

Fig. S9 (a) N_2 adsorption isotherms and (b) pore size distributions of a-rGO, TAPT-DHTA-COF and a-rGO@TD-COF-4.

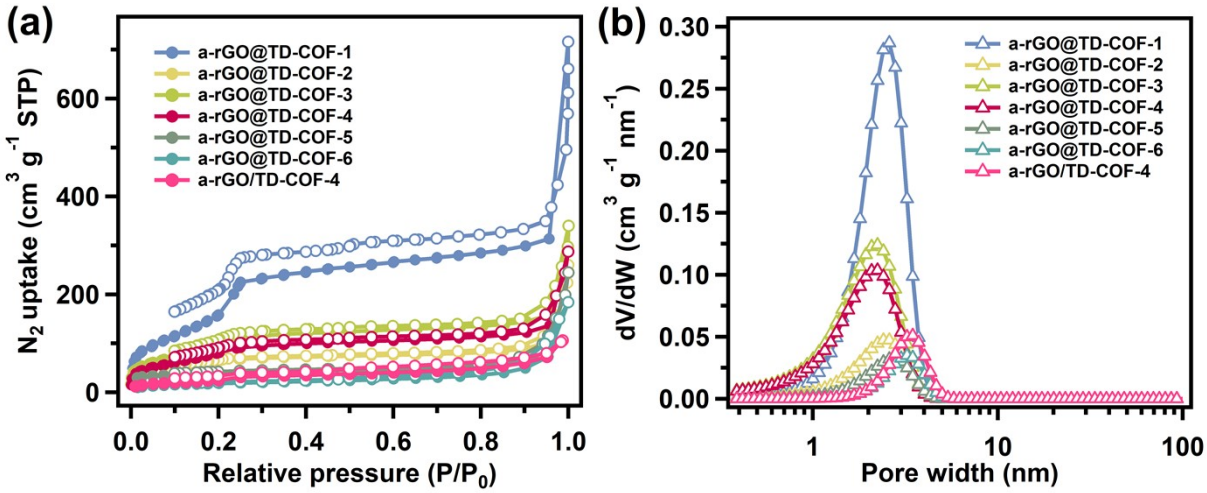

Fig. S10 (a) N_2 adsorption isotherms and (b) pore size distributions of a-rGO@TD-COF-1-6 and a-rGO/TD-COF-4.

Section J. CV and GCD curves

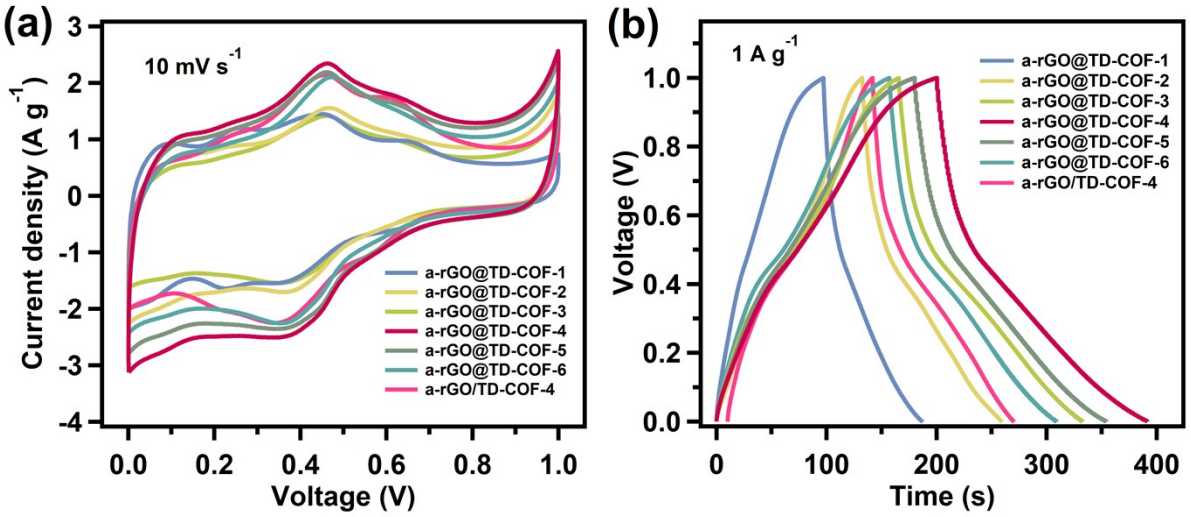

Fig. S11 (a) CV curves at 10 mV s^{-1} and (b) GCD curves at 1 A g^{-1} of a-rGO/TD-COF-4 and a-rGO@TD-COF-1-6.

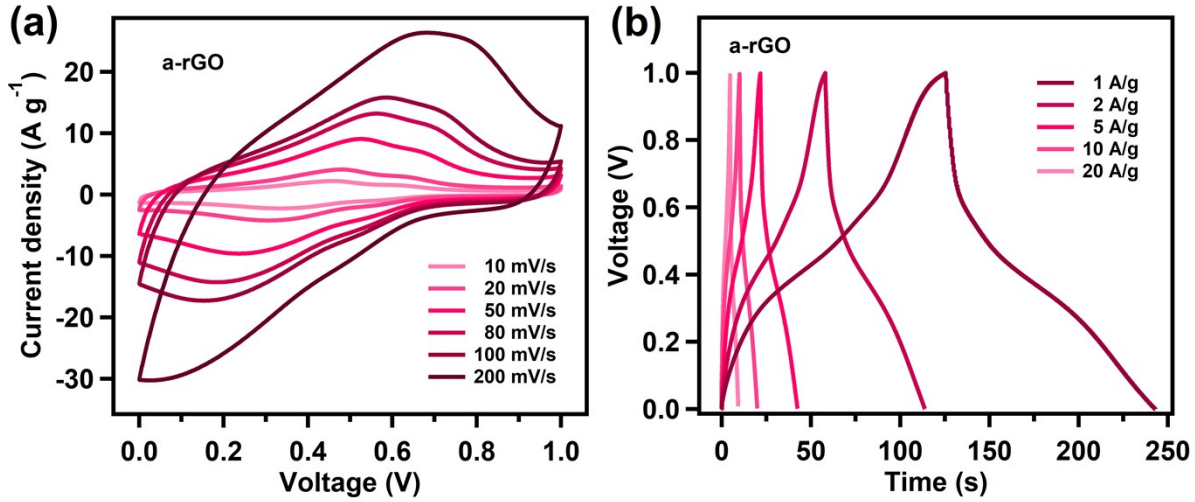

Fig. S12 (a) CV and (b) GCD curves of a-rGO measured in the three-electrode configuration under different scan rates and charging/discharging densities.

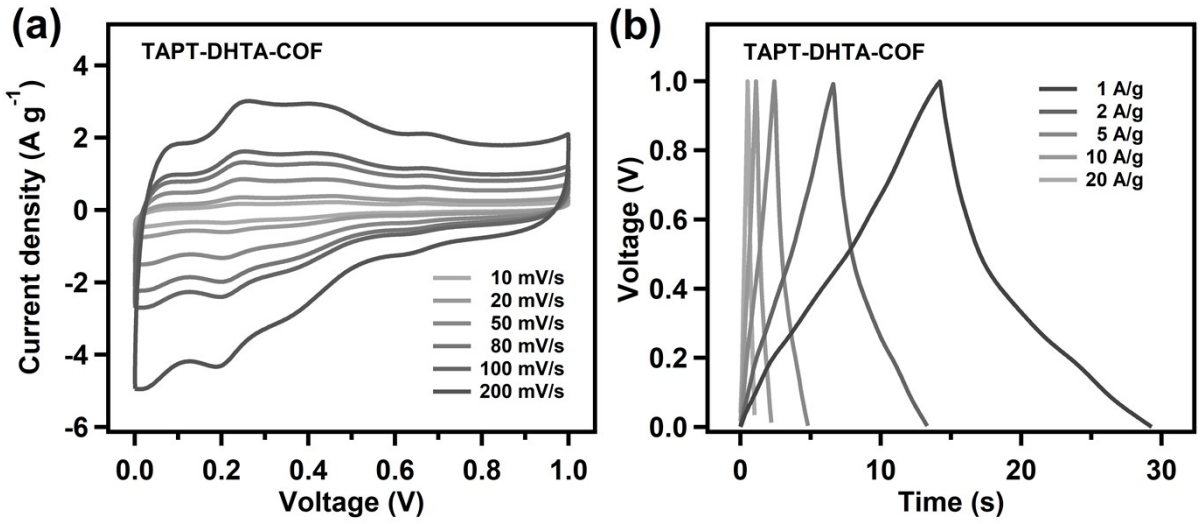

Fig. S13 (a) CV and (b) GCD curves of TAPT-DHTA-COF measured in the three-electrode configuration under different scan rates and charging/discharging densities.

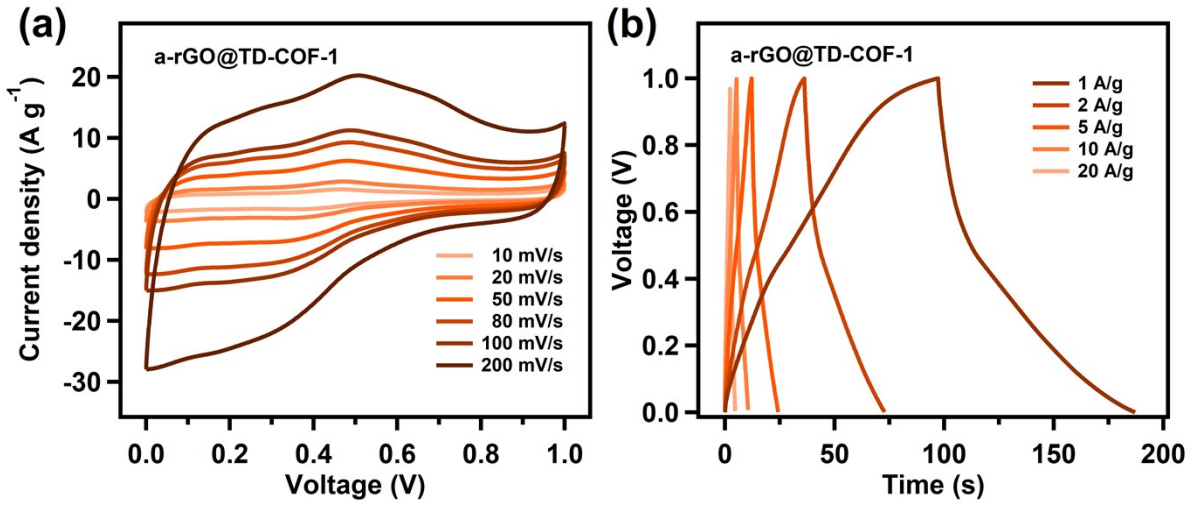

Fig. S14 (a) CV and (b) GCD curves of a-rGO@TD-COF-1 measured in the three-electrode configuration under different scan rates and charging/discharging densities.

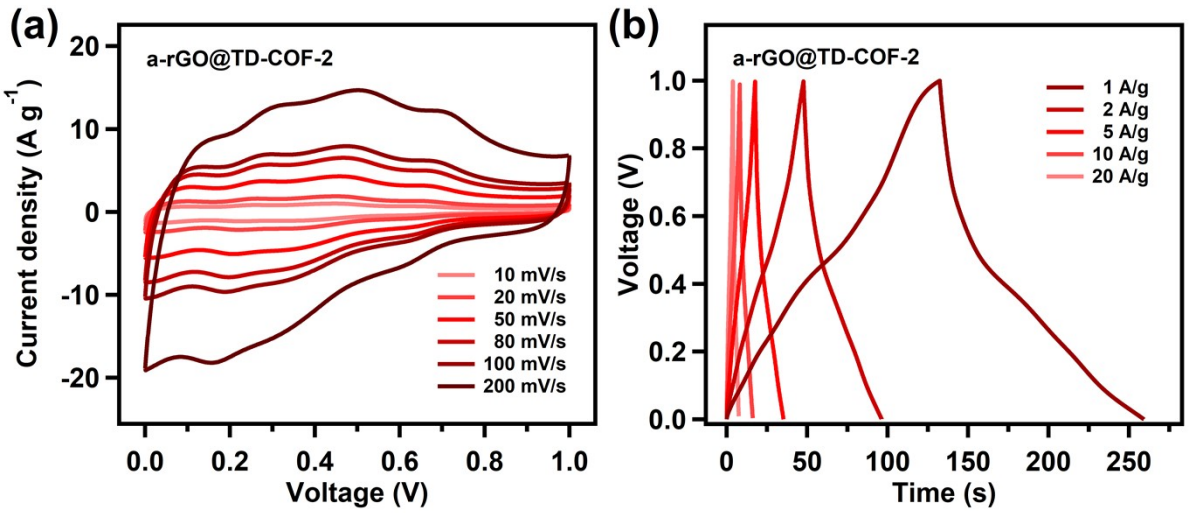

Fig. S15 (a) CV and (b) GCD curves of a-rGO@TD-COF-2 measured in the three-electrode configuration under different scan rates and charging/discharging densities.

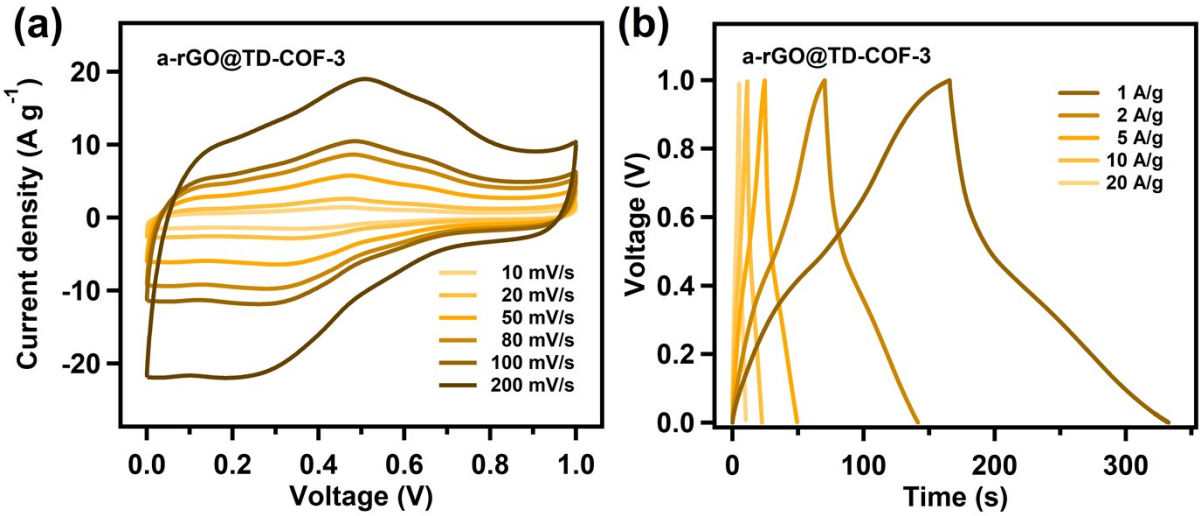

Fig. S16 (a) CV and (b) GCD curves of a-rGO@TD-COF-3 measured in the three-electrode configuration under different scan rates and charging/discharging densities.

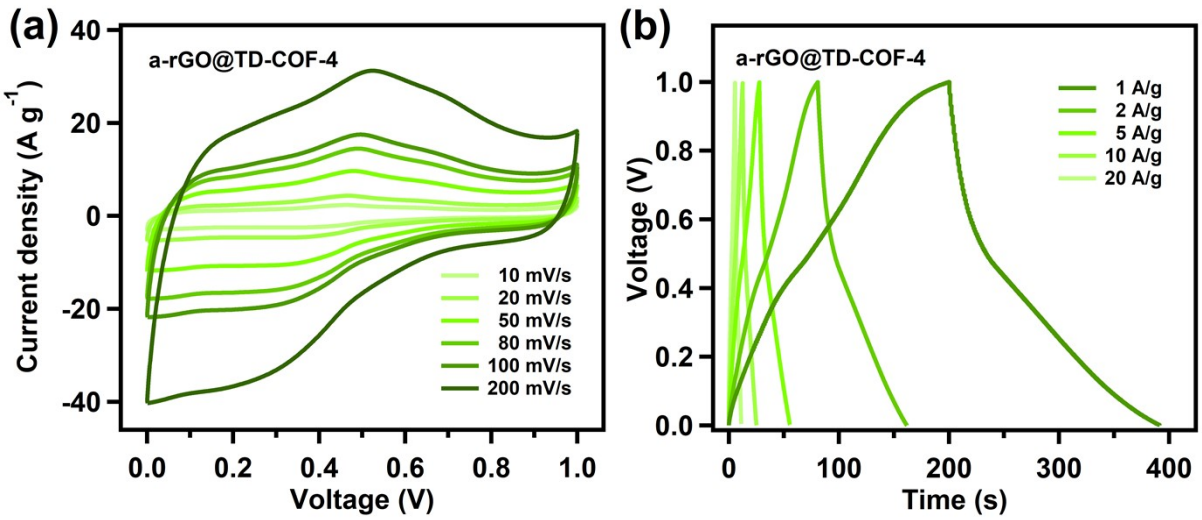

Fig. S17 (a) CV and (b) GCD curves of a-rGO@TD-COF-4 measured in the three-electrode configuration under different scan rates and charging/discharging densities.

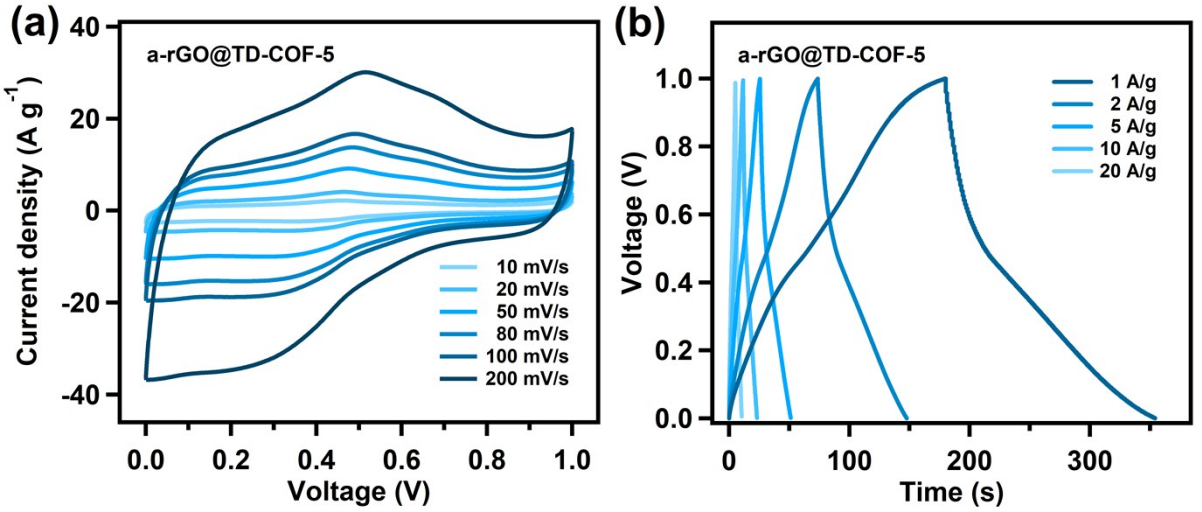

Fig. S18 (a) CV and (b) GCD curves of a-rGO@TD-COF-5 measured in the three-electrode configuration under different scan rates and charging/discharging densities.

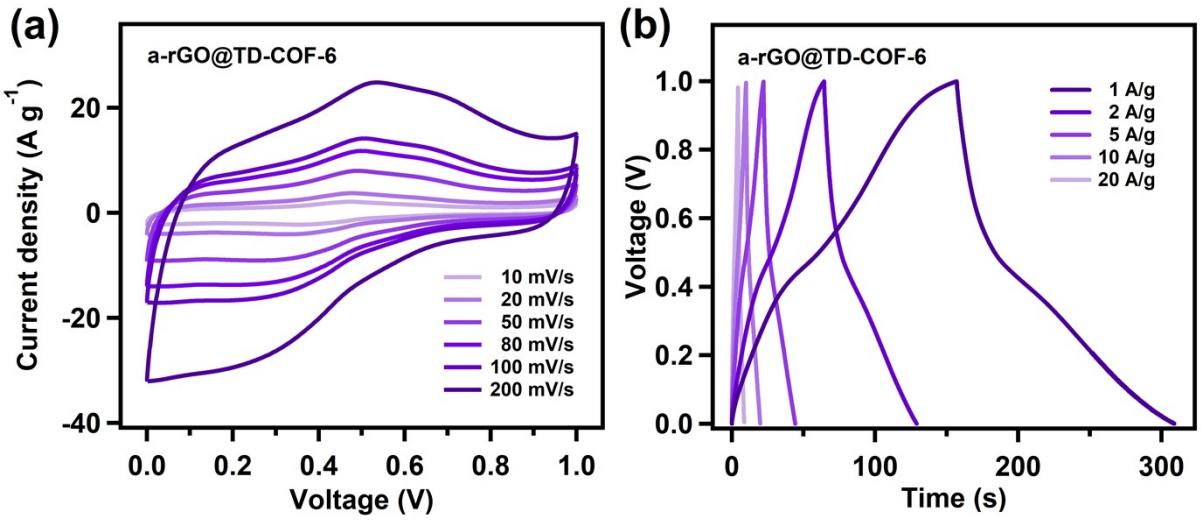

Fig. S19 (a) CV and (b) GCD curves of a-rGO@TD-COF-6 measured in the three-electrode configuration under different scan rates and charging/discharging densities.

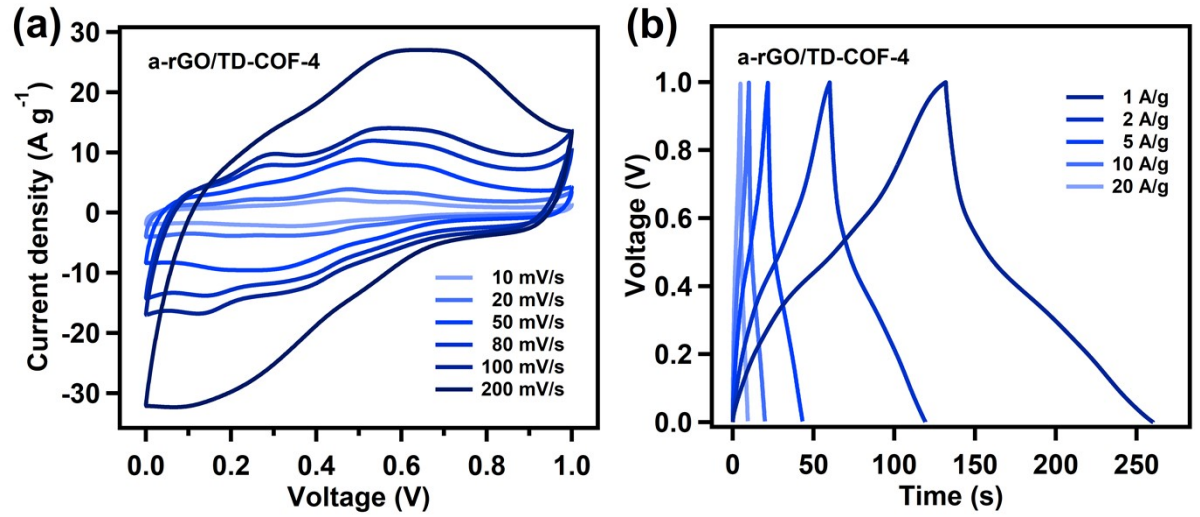

Fig. S20 (a) CV and (b) GCD curves of a-rGO/TD-COF-4 measured in the three-electrode configuration under different scan rates and charging/discharging densities.

Section K. EIS measurements

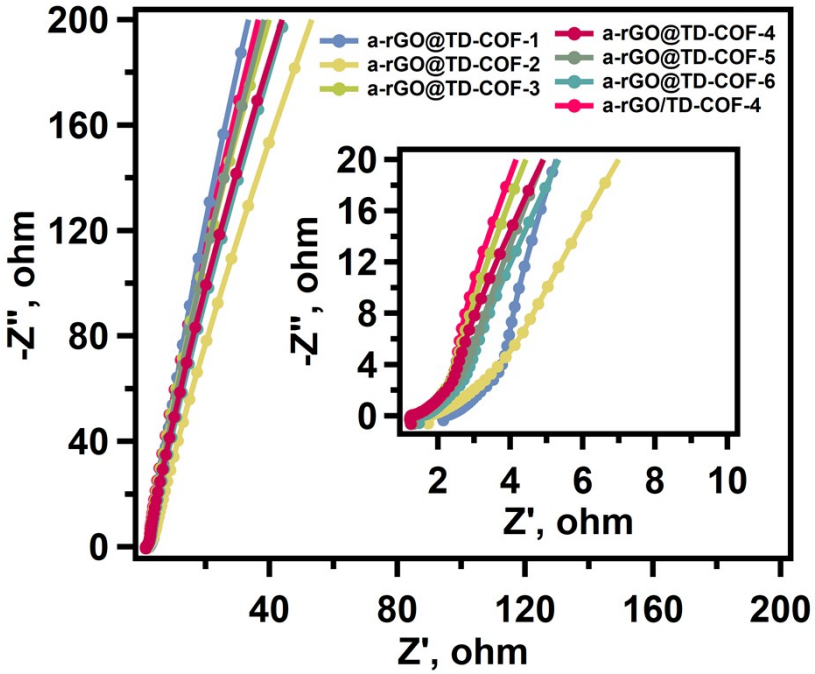

Fig. S21 Nyquist plots of a-rGO/TD-COF-4 and a-rGO@TD-COF-1-6 (Inset: the magnified high-frequency region).

Table S1 Porosity properties, gas uptake and specific capacitance for the materials.

Composite materials	S_{BET}[a] ($m^2\ g^{-1}$)	V_{total}[b] ($cm^3\ g^{-1}$)	Pore size (nm)	C_m[c] ($F\ g^{-1}$)
a-rGO	50	0.13	14.0	116
TAPT-DHTA-COF	1554	1.24	2.6	15
a-rGO@TD-COF-1	717	0.97	2.8	90
a-rGO@TD-COF-2	170	0.30	2.8	128
a-rGO@TD-COF-3	378	0.46	2.6	162
a-rGO@TD-COF-4	302	0.39	2.6	195
a-rGO@TD-COF-5	76	0.29	3.0	170
a-rGO@TD-COF-6	65	0.24	3.7	155
a-rGO/TD-COF-4	80	0.16	3.4	129

[a] Surface area calculated by the BET method; [b] Total pore volume at $P/P_0 \sim 0.995$; [c] Current density at 1 A g^{-1}

Table S2 Performance comparison of the a-rGO@TD-COF-4 hybrid with some recently reported COFs and GO composites (All tested were performed using the three-electrode configuration in aqueous electrolytes).

Electrodes	Electrolyte	Current density, A g^{-1}	C_m, F g^{-1}	Times	Ref.
a-rGO@TD-COF-4	1 M H_2SO_4	1	195	13	This work
TAPT-DHTA-COF	1 M H_2SO_4	1	15	--	This work
a-rGO	1 M H_2SO_4	1	110	--	This work
DAAQ-COFs/GA	1 M H_2SO_4	1	378	24	4
rGO/COF-20	1 M H_2SO_4	1	321	32	5
COFs/NH_2–rGO	1 M Na_2SO_4	0.2	533	3	6
COF/rGO-30	1 M H_2SO_4	0.5	599	5	7
$COF_{BTA\text{-}DPPD}$–rGO	2 M KOH	0.5	239	4	8
NH_2-f-MWCNT@$COF_{TTA–DHTA}$	1 M Na_2SO_4	0.4	127.5	12	9
CNT@TFA-COF-3	1 M H_2SO_4	1	338	8.5	10
a-GO@COF-F-5	1 M H_2SO_4	1	295	4	11

Section L. Supporting references

1. X. K. Zhang, H. Li, J. Wang, D. L. Peng, J. D. Liu and Y. T. Zhang, *J. Membr. Sci.*, 2019, **581**, 321-330.
2. J. Geng and H.-T. Jung, *The Journal of Physical Chemistry C*, 2010, **114**, 8227-8234.
3. W. J. Yang, H. H. Zhou, Z. Huang, H. X. Li, C. P. Fu, L. Chen, M. B. Li, S. S. Liu and Y. F. Kuang, *Electrochim. Acta*, 2017, **245**, 41-50.
4. N. An, Z. Guo, J. Xin, Y. He, K. Xie, D. Sun, X. Dong and Z. Hu, *J. Mater. Chem. A*, 2021, **9**, 16824-16833.
5. C. Wang, F. Liu, J. Chen, Z. Yuan, C. Liu, X. Zhang, M. Xu, L. Wei and Y. Chen, *Energy Storage Materials*, 2020, **32**, 448-457.
6. P. Wang, Q. Wu, L. Han, S. Wang, S. Fang, Z. Zhang and S. Sun, *RSC Adv.*, 2015, **5**, 27290-27294.
7. C. J. Wang, F. Liu, S. J. Yan, C. Liu, Z. X. Yu, J. S. Chen, R. Lyu, Z. Y. Wang, M. Y. Xu, S. L. Dai, Y. Chen and L. Wei, *Carbon*, 2022, **190**, 412-421.
8. L. R. Xu, F. Wang, X. Ge, R. Y. Liu, M. Xu and J. Q. Yang, *Microporous Mesoporous Mat.*, 2019, **287**, 65-70.
9. B. Sun, J. Liu, A. Cao, W. Song and D. Wang, *Chem Commun*, 2017, **53**, 6303-6306.
10. L. Liu, D. Cui, S. Zhang, W. Xie, C. Yao and Y. Xu, *Dalton Trans*, 2023, **52**, 2762-2769.
11. D. Cui, W. Xie, S. Zhang, Y. Xu and Z. Su, *Polym. Chem.*, 2023, **14**, 803-810.